Eur. Phys. J. D **31**, 165–177 (2004)
DOI: 10.1140/epjd/e2004-00162-7

THE EUROPEAN PHYSICAL JOURNAL D

The photoassociative spectroscopy, photoassociative molecule formation, and trapping of ultracold $^{39}K^{85}Rb$

D. Wang[1], J. Qi[1], M.F. Stone[1], O. Nikolayeva[2], B. Hattaway[1], S.D. Gensemer[3], H. Wang[4], W.T. Zemke[5], P.L. Gould[1], E.E. Eyler[1], and W.C. Stwalley[1,a]

[1] Department of Physics, University of Connecticut, 2152 Hillside Road, Storrs, CT 06269-3046, USA
[2] Department of Physics, University of Latvia, 19 Rainis Boulevard, Riga 15986, Latvia
[3] Department of Physics, University of Amsterdam, P.O. Box 94604, 1090 GP, Amsterdam, The Netherlands
[4] Electronics and Photonics Laboratory, The Aerospace Corporation, M2-253, 2350 East El Segundo Boulevard, El Segundo, CA 90245-4691, USA
[5] Department of Chemistry, Wartburg College, Waverly, IA 50677, USA

Received 22 September 2004
Published online 23 November 2004 –

Abstract. We have observed the photoassociative spectra of colliding ultracold ^{39}K and ^{85}Rb atoms to produce KRb* in all eight bound electronic states correlating with the ^{39}K ($4s$) + ^{85}Rb($5p_{1/2}$ and $5p_{3/2}$) asymptotes. These electronically excited KRb* ultracold molecules are detected after their radiative decay to the metastable triplet ($a^3\Sigma^+$) state and (in some cases) the singlet ($X^1\Sigma^+$) ground state. The triplet ($a^3\Sigma^+$) ultracold molecules are detected by two-photon ionization at 602.5 nm to form KRb^+, followed by time-of-flight mass spectroscopy. We are able to assign a majority of the spectrum to three states ($2(0^+)$, $2(0^-)$, $2(1)$) in a lower triad of states with similar C_6 values correlating to the K($4s$) + Rb ($5p_{1/2}$) asymptote; and to five states in an upper triad of three states ($3(0^+)$, $3(0^-)$, $3(1)$) and a dyad of two states ($4(1)$, $1(2)$), with one set of similar C_6 values within the upper triad and a different set of similar C_6 values within the dyad. We are also able to make connection with the short-range spectra of Kasahara et al. [J. Chem. Phys. **111**, 8857 (1999)], identifying three of our levels as $v = 61$, 62 and 63 of the $1^1\Pi \sim 4(1)$ state they observed. We also argue that ultracold photoassociation to levels between the K($4s$) + Rb ($5p_{3/2}$) and K($4s$) + Rb ($5p_{1/2}$) asymptotes may be weakly or strongly predissociated and therefore difficult to observe by ionization of $a^3\Sigma^+$ (or $X^1\Sigma^+$) molecules; we do know from Kasahara et al. that levels of the $1^1\Pi \sim 4(1)$ and $2^1\Pi \sim 5(1)$ states in the intra-asymptote region are predissociated. A small fraction ($\leq 1/3$) of the triplet ($a^3\Sigma^+$) ultracold molecules formed are trapped in the weak magnetic field of our magneto-optical trap (MOT).

PACS. 33.20.Fb Raman and Rayleigh spectra (including optical scattering) – 34.20.Cf Interatomic potentials and forces – 33.80.Ps Optical cooling of molecules; trapping

1 Introduction

The use of ultracold ($T < 1$ mK) gas phase techniques [1] has revolutionized atomic physics and led to recent Nobel Prizes in atom cooling and trapping [2–4] and atomic Bose-Einstein condensation (BEC) [5,6]. Starting with the observation of ultracold Cs_2 molecules [7], a similar revolution is sweeping molecular physics. The formation and trapping of molecules at translational temperatures below 1 K has been an area of great interest for many reasons: quantum degeneracy, quantum and resonant collisions, precision spectroscopy, molecule optics, quantum information, etc. [8].

A particularly promising ultracold molecule formation process is photoassociation (PA) of ultracold atoms [9,10]. However, nearly all such work has involved photoassociation of two atoms of the same isotopic species to form a homonuclear nonpolar molecule. PA of a single heteronuclear nonpolar molecule, ^{6}Li^{7}Li, has also been observed [11].

In several cases, the resulting homonuclear molecules have been trapped [12,13]. Feshbach resonances have been used in colder atom samples (usually in optical traps) to form very weakly bound homonuclear molecules via magnetic tuning in Cs_2 [14,15], Rb_2 [16], Na_2 [17], Li_2 [18–21] and K_2 [22,23]. The weakly bound levels of $^6Li_2$ and $^{40}K_2$ showed remarkably long lifetimes, which led to the achievement of molecular BEC for both $^6Li_2$ [18,21] and $^{40}K_2$ [23]. The long lifetimes were attributed primarily to "Pauli Blocking" for fermions [24], although slow relaxation of the uppermost vibrational levels at ultracold

[a] e-mail: w.stwalley@uconn.edu

temperatures may also be a factor [25–27]. One of the major challenges now is to convert molecules in such a Feshbach-resonance-produced weakly bound level into molecules in the $v = 0$, $J = 0$ level of the $X^1\Sigma_g^+$ ground state.

Among the heteronuclear alkali dimers, it was predicted that KRb would be the most promising candidate for PA to form a heteronuclear polar molecule, followed by RbCs and KCs [28]. This is because the $K(4p_J)$ and $Rb(5p_J)$ levels are nearly degenerate, giving rise to particularly large C_6 values (both positive and negative) at the K^* + Rb and K + Rb^* limits. Recently, Kerman et al. have reported PA spectra of $^{85}Rb^{133}Cs$ [29] and detection of the corresponding triplet ($a^3\Sigma^+$) ultracold RbCs molecules [30]. A discussion of prospects for producing singlet ($X^1\Sigma^+$) ultracold RbCs molecules is included in this issue of Eur. Phys. J. D [31].

We note that previously $NaCs^+$ [32], RbCs [33], and KRb [34] have been detected in cold atom traps, but without assigned PA spectra and without establishing the molecular formation mechanism. In very recent experiments, Feshbach resonances have been reported in K + Rb [35] and Li + Na [36], so we expect that efficient processes for forming ultracold heteronuclear molecules will be increasingly explored. It has also been proposed that stimulated Raman scattering through intermediate states of mixed singlet-triplet character can efficiently and state-selectively convert these Feshbach-resonance-produced weakly bound molecules into $X^1\Sigma^+$ $v = 0$, $J = 0$ molecules [27,31]. This same process will not work as simply in homonuclear molecules because of the gerade-ungerade selection rule. We note that at higher temperatures (>10 mK), CaH has been buffer-gas cooled and magnetically trapped [37], while ND_3 has been electrostatically decelerated and loaded into electric traps [38,39].

Here we report in detail the photoassociative spectra, photoassociative molecule formation, and the trapping of the heteronuclear polar ultracold molecule $^{39}K^{85}Rb$. A brief summary was previously submitted [40].

In the following sections, we first review prior experimental and theoretical work on the KRb molecule at all temperatures (Sect. 2). Then we discuss our experimental apparatus and procedures (Sect. 3). In Section 4 we discuss the photoassociative spectra and the photoassociative molecule formation process. Magnetic trapping of KRb molecules in the metastable $a^3\Sigma^+$ state is then discussed (Sect. 5). Future prospects for ultracold KRb studies are discussed in Section 6.

2 Review of prior work on KRb

The KRb molecule was poorly understood and characterized before 1990. It was first observed in diffuse spectra (peaking near 496 nm) in 1928 [41]. This is the only spectroscopic experiment mentioned in the 1979 compilation of diatomic molecule spectra by Huber and Herzberg [42]. KRb was directly observed in pioneering studies of alkali atom-alkali dimer exchange reactions in 1973 [43]. A second set of diffuse spectra (peaking at 567, 586.7 and 597 nm) was assigned to KRb in 1984 [44]; a third set (peaking at 730.07, 732.10, 734.74 and 755.51 nm) assigned to KRb in 2002 is the most relevant to the present work [45].

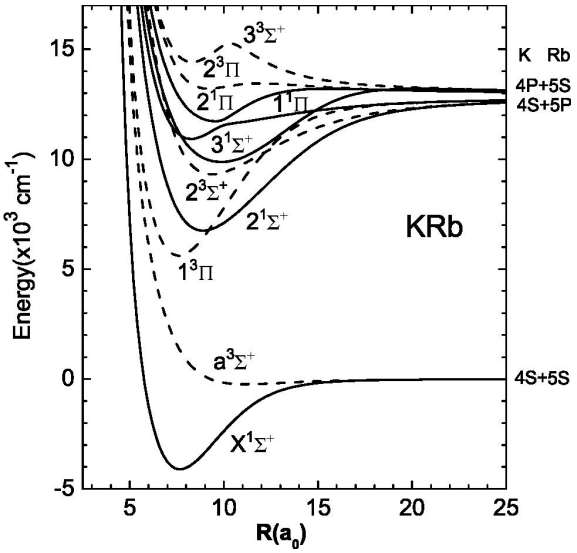

Fig. 1. Potential energy curves (in 10^3 cm^{-1} versus R in a_0) of the KRb molecule based on the high quality ab initio calculations of [55].

High resolution spectroscopic studies began with the pioneering work of Ross et al. on the $A^1\Sigma^+ - X^1\Sigma^+$ bands [46]. Impressive results followed on the $1(B)^1\Pi$ [47,48], the $2^1\Pi$ [48,49], the $X^1\Sigma^+$ [50], the $3^1\Pi$ and $3^1\Sigma^+$ [51], the $2^3\Sigma^+$ [52], and the $1^1\Delta$ states [53] of KRb, including observations and analysis of interactions with a number of other states. The $2^1\Pi$ state vibrational numbering has been corrected [49] and the predissociation of the $1^1\Pi$ and $2^1\Pi$ states by the $2^3\Sigma^+$ state has been observed [48] and used to obtain a precise dissociation energy $D_e = 4217.91 \pm 0.42$ cm^{-1} [54]. Accurate experimentally-based potential energy curves are available for portions of the $X^1\Sigma^+$ [50], $1^1\Pi$ [48], $2^1\Pi$ [49], $3^1\Sigma^+$ [51], $2^3\Sigma^+$ [52], and $1^1\Delta$ states [53]. Levels in the neighborhood of our photoassociative spectra (up to 95 cm^{-1} below the $K(4s)$ + $Rb(5p_{1/2})$ asymptote) were previously estimated in [48] and are given in Table 1. We believe we have also observed the $v = 61-63$ levels of the $1^1\Pi \sim 4(1)$ state.

While there are a number of interesting earlier theoretical studies of KRb potential curves and of other electronic properties (e.g. dipole moment, transition dipole moment, ionization potential), we are now in the enviable position of having three sets of high quality theoretical potential energy curves available [55–57]. These curves are generally in very good agreement with experiment. We show the results of [55] in Figure 1. To give an indication of the high quality of the curves, we show in Table 2 a comparison of the three calculations for the $a^3\Sigma^+$ potential, one of the two lower states from which PA occurs and the molecular state from which we know we are producing KRb^+ ions by two-photon ionization at 602.5 nm. It is

$1^1\Pi \sim 4$ (1)				$2^1\Pi \sim 5$ (1)			
v	T_v	$10^3 B_v$	E_v	v	T_v	$10^3 B_v$	E_v
56	16698.612	14.614	98.30				
57*	16710.506	15.357	86.40	16*	16709.506	21.78	87.40
58	16726.444	14.329	70.47				
59	16739.531	13.911	57.38				
60*	16751.793	13.875	45.12	17*	16752.540	20.80	44.37
61	16765.427	13.919	31.48				
62	16777.684	13.256	19.23				
63	16789.030	13.630	7.88				
64*	16801.448	14.403	–4.54	18*	16796.987	20.21	–0.08

Table 1. Vibrational energy levels T_v (in cm^{-1}), with $10^3 B_v$ (in cm^{-1}) previously estimated from higher J levels by Kasahara et al. [48] within the last 100 cm^{-1} below the $^{39}K(4s)$ + $^{85}Rb(5p_{1/2})$ limit ($F'' = 2 \rightarrow F' = 2$) at 12579.00043 (1) cm^{-1} with respect to ground state atoms and at 16796.91 (42) cm^{-1} with respect to the minimum of the ground $X^1\Sigma^+$ state. The binding energies E_v (uncertain by 0.42 cm^{-1}) are also given. Perturbing levels at low J are indicated with asterisks. Levels observed by photoassociation are underlined. The vibrational quantum numbers of the $2^1\Pi \sim 5$ (1) state have been renumbered as determined by Amiot et al. [49].

Table 2. Asymptotic behavior of the potential energy of the $a^3\Sigma^+$ triplet state from ab initio calculations [55–57] compared with the long-range sum of dispersion plus exchange long-range interactions [61]. ΔV (cm^{-1}) is the potential energy with respect to the dissociation limit; R is the internuclear distance in atomic units (Bohr).

R	$-\Delta V$			
	[55]	[56]	[57]	[61]
16	77.0	76.8781	75.2710	75.5010
20	25.0	22.4653	19.4370	19.5651
24	10.0	7.4532	6.0574	6.0897
28	5.0	2.7286	2.2696	2.2791
32	3.0	1.2112	0.9810	0.9843
36	2.0	0.6752	0.4718	0.4731
40	1.0	0.4354	0.2463	0.2468
50	0.0	0.1035	0.0629	0.0629

also the state trapped in our work. As shown in Table 2, the work of [55] suffers from lack of significant figures at large R. The work of [56] agrees relatively well with the asymptotically correct sum of dispersion [58,59] plus exchange potentials [60,61], but the agreement of [57] with the latter is truly remarkable (within 1%).

It is worth noting that a variety of calculations have been carried out for dispersion interactions (Tab. 3), not only for ground state atoms [58,59,62,63], but also for excited atoms [62,64]. This is particularly important for the K^* + Rb and Rb^* + K limits, since the coefficients are especially large because of the near degeneracy of K^* and Rb^* levels. Unfortunately, the calculations of [62] do not include spin-orbit effects. Our PA experiments below allow estimates of C_6 for the $2(0^+)$, $2(0^-)$ and 2(1) "triad" of states, with similar C_6 coefficients, as predicted theoretically. It is worth noting that for the states correlating with $K(4s)$ + $Rb(5p_{3/2})$, there is another "triad" of states with similar C_6 values ($3(0^+)$, $3(0^-)$, 3(1)) and a "dyad" of states (4(1), 1(2)) with similar C_6 values, different from those of the $3(0^+)$, $3(0^-)$, 3(1) triad. Figures 2 and 3 nicely illustrate this lower triad, upper triad, and dyad structure of the potential curves.

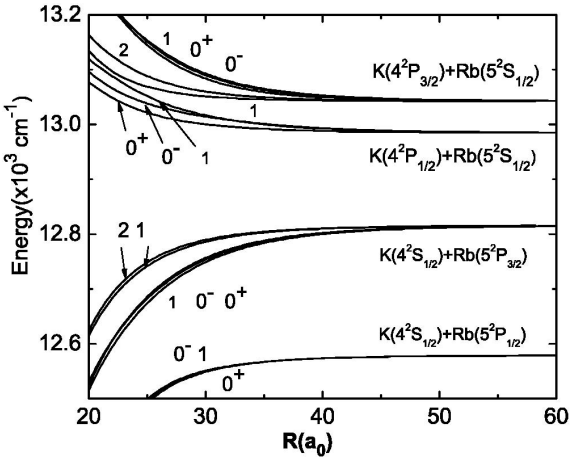

Fig. 2. The 16 excited long-range Hund's case (c) potential energy curves of KRb at the $K(4p_J)$ + $Rb(5s)$ and $K(4s)$ + $Rb(5p_J)$ asymptotes [28]. Note that potentials at the two lower asymptotes are attractive while those at the two upper asymptotes are repulsive.

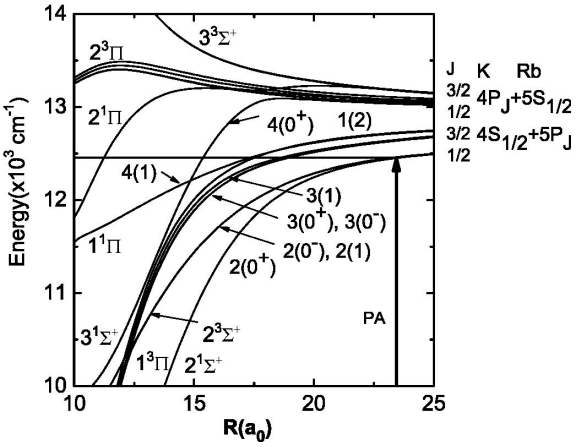

Fig. 3. Correlation at intermediate distances of the potential curves of the short-range states in Figure 1 ($^{2S+1}\Lambda^{(\pm)}$) with the potential curves of the long-range states ($\Omega^{(\pm)}$) in Figure 2. The states are numbered in order of increasing energy. Also shown is the approximate minimum PA distance ($\sim 23a_0$) corresponding to a level detuned 95 cm^{-1} below the $K(4s)$ + $Rb(5p_{1/2})$ asymptote.

Table 3. Long range dispersion coefficients C_6, C_8 and C_{10} for various asymptotes of KRb, all in atomic units. Recommended values are asterisked.

Asymptote	State	C_6 ($\times 10^5$)	C_8 ($\times 10^7$)	C_{10} ($\times 10^9$)	Reference
K($4s$) + Rb($5s$)	$1(0^+)$, $1(0^-)$, 1(1)	0.04106	0.04760	0.06352	[62]
		0.04274*	—	—	[58]
		—	0.04930*	0.06300*	[59]
K($4s$) + Rb($5p_{1/2}$)	$2(0^+)$	0.8770	—	—	[64]
		1.0311*	1.8173*	—	[65]
	$2(0^-)$	0.7875	—	—	[64]
		0.9127*	1.8548*		[65]
	2(1)	0.8099	—	—	[64]
		0.9384*	1.9220*	—	[65]
K($4s$) + Rb($5p_{3/2}$)	$3(0^+)$	2.325	—	—	[64]
		3.063*	1.152*	—	[65]
	$3(0^-)$	2.762	—	—	[64]
		3.628*	1.190*	—	[65]
	3(1)	2.514	—	—	[64]
		3.310*	1.257*	—	[65]
	4(1)	0.9367	—	—	[64]
		1.205*	0.2728*	—	[65]
	1(2)	0.7944	—	—	[64]
		1.024*	0.2769*	—	[65]

Other electronic properties are also of importance. Since K and Rb are the most similar of the alkali atoms, we expect a small dipole moment, which is found in the ab initio calculations. Our calculation of radiative transition probabilities within the $X^1\Sigma^+$ state [60], using a hybrid (experimental and theoretical) potential and the dipole moment function of [56], predicted radiative lifetimes $\geq 10^3$ seconds, far too long to be important in the current generation of KRb experiments. Changing to the dipole moment function of [57] showed only minor differences and again no radiative lifetimes $< 10^3$ seconds [63].

The transition dipole moment functions from intermediate range to the long-range Hund's case (c) limit are available for certain states in the ab initio calculations of [57]. These calculations bear directly on our experiments discussed below and are thus discussed here. First note the long-range potentials shown in Figure 2 [28], based on the theoretical calculations of Bussery et al. [65] (which are about 10% more attractive than the earlier calculation of Movre and Beuc [64] and 30% more attractive than the later calculations of Marinescu and Sadeghpour [62]). The intermediate range connection between Figures 1 and 2, based on the correlation diagram of [28] and the results of [57], is shown in Figure 3. Since our PA spectra are detuned by no more than 95 cm^{-1} below the K($4s$) + Rb($5p_{1/2}$) limit, we see that PA occurs predominantly to the lower triad of states ($2(0^+)$, $2(0^-)$, 2(1)) with outer classical turning points (and Condon points) outside $\sim 23a_0$.

However, the upper triad of states ($3(0^+)$, $3(0^-)$, 3(1)), and the dyad of states (4(1), 1(2)) correlated with the K($4s$) + Rb($5p_{3/2}$) limit are also excited, having outer turning points (and Condon points) at only slightly smaller distance ($\geq 17a_0$). It is even conceivable that other states could be observed, e.g. the $2^1\Pi \sim 5(1)$ state in Table 1 and the $4(0^+)$ state in Figure 3, but we have no evidence of such at this point. With the transition moments of [57], we can estimate the branching ratio of singlet and triplet spontaneous emission from levels formed by PA and correlating with the K($4s$) + Rb($5p_J$) asymptotes. Taking $50a_0$ as a typical PA distance ($\sim$upper level outer turning point and transition Condon point), one estimates the branching fractions shown in Table 4. Note in particular that while some states ($2(0^-)$, $3(0^-)$, 1(2)) give

Table 4. Asymptotic ($\sim 50a_0$) relative singlet ($\rightarrow 1(0^+) \sim X^1\Sigma^+$) and triplet ($\rightarrow 1(0^-)$ and $1(1) \sim a^3\Sigma^+$) spontaneous emission from various Hund's case (c) states correlating with the K($4s$) + Rb($5p_J$) asymptotes.

		fraction	
asymptote	upper state	singlet	triplet
$4s + 5p_{1/2}$	$2(0^+)$	0.18	0.82
	$2(0^-)$	0.00	1.00
	2(1)	0.22	0.78
$4s + 5p_{3/2}$	$3(0^+)$	$\sim$0.25*	$\sim$0.75*
	$3(0^-)$	0.00	1.00
	3(1)	$\sim$0.25*	$\sim$0.75*
	4(1)	$\sim$0.25*	$\sim$0.75*
	1(2)	0.00	1.00

*Statistical; transition moments not available.

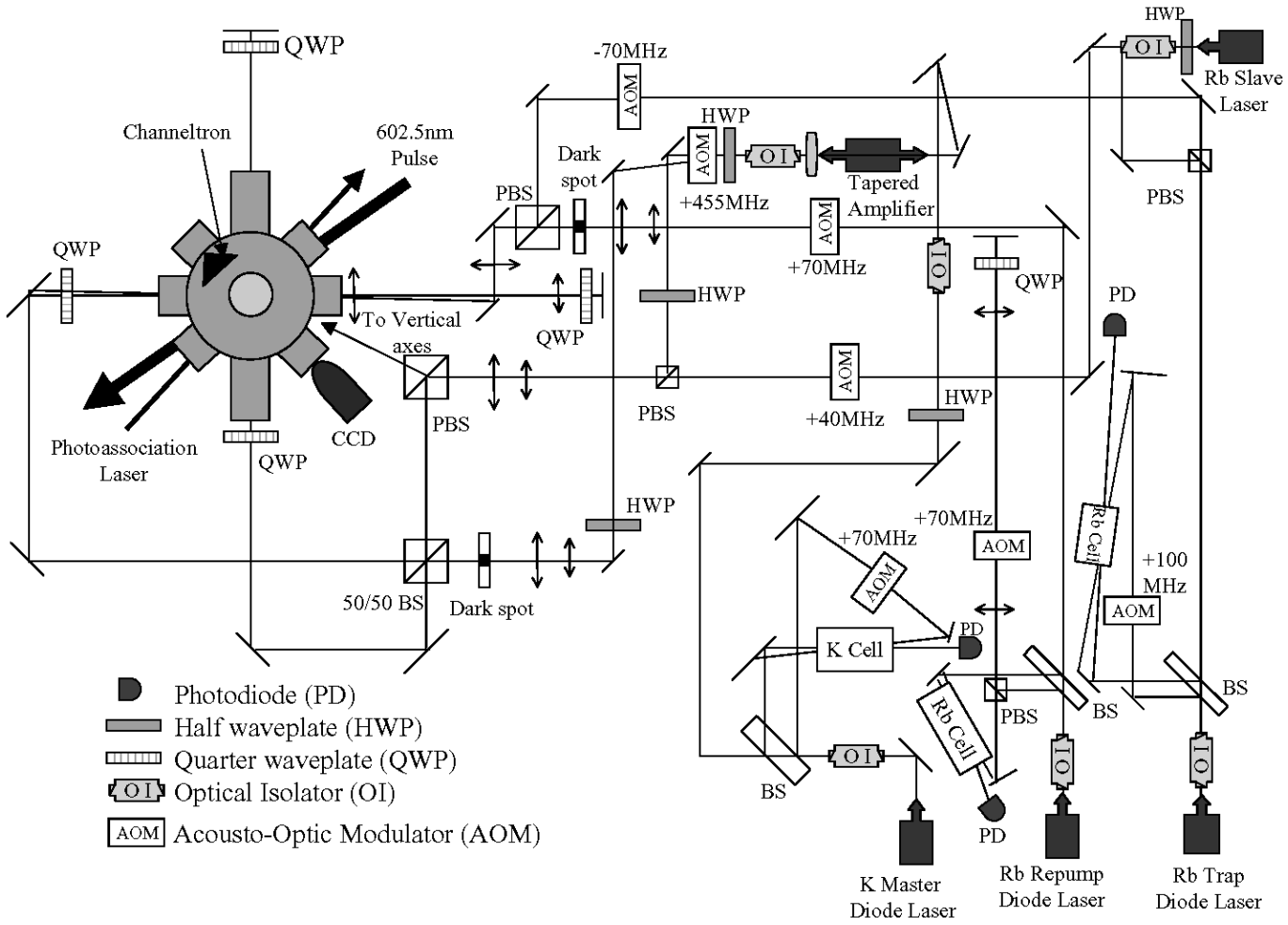

Fig. 4. Schematic diagram of the dual species ^{39}K/^{85}Rb MOT apparatus used in our PA spectroscopy/molecule formation and trapping experiments. The KRb dual dark-spot MOTs were produced at the center of the chamber and the pressure of the ten-arm stainless vacuum chamber (left side) was about 5×10^{-10} Torr without the presence of K and Rb vapors. The K and Rb MOT laser beams were combined with polarized cubes and one set of MOT optics was used for both K and Rb. The total power for the K MOT is about 350 mW and was obtained by injecting the K master laser beam into a Toptica tapered amplifier. The trap beams used 300 mW and the remaining 50 mW for the repump was 455 MHz blue shifted with respect to the trap beam by an AOM. The Rb master laser beam was split into two beams; one was injected into a Rb slave laser to produce a 40 mW trap beam and one was used for the depump beam. The Rb repump beam was about 4 mW and obtained from a separate Rb diode laser. PD: photodiode; HWP: Half Waveplate; QWP: Quarter Waveplate; OI: Optical Isolator; AOM: Acousto-optic Modulator; BS: Beam splitter.

exclusively triplet emission, *all* states probably give predominantly triplet emission. This implies that PA spectra of all eight states can be obtained by detection of only triplet molecules, which we are confident we detect in our experiments. It also implies that it may be somewhat difficult to efficiently produce singlet ground state molecules, since they probably represent a relatively minor decay channel for each upper state. This is in stark contrast to homonuclear PA, where spontaneous emission from gerade (g) states is 100% triplet and from ungerade (u) states is 100% singlet [9].

We also note that the collisions of K and Rb have been extensively studied both at high temperatures (e.g. [66–68]) and at ultracold temperatures (e.g. [34,69–72]). However, we do not discuss these studies in detail here.

3 Experimental apparatus and procedures

Our dual species ^{39}K/^{85}Rb MOT [73] is based on the addition of ^{85}Rb trapping and repump beams to our former ^{39}K MOT [74]. The apparatus schematic is shown in Figure 4. Because of the closeness of the K and Rb resonance transitions, the K and Rb diode laser beams frequently share optics. Normally, both the ^{39}K and the ^{85}Rb MOTs are operated as "dark spot" MOTs [75]. Typical densities are 3×10^{10} cm^{-3} for K and 1×10^{11} cm^{-3} for Rb. The individual MOTs are expected to have typical temperatures of

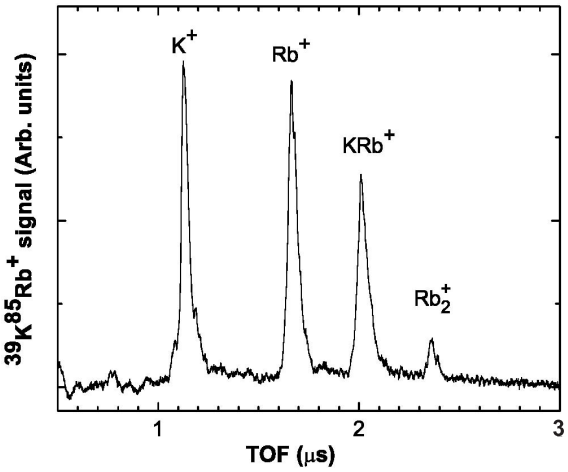

Fig. 5. Typical time-of-flight mass spectrum for 602.5 nm two-photon ionization for the PA laser tuned 39.80 cm^{-1} below the Rb ($5p_{1/2}$ $F' = 2 \rightarrow 5s$ $F'' = 2$) line, corresponding to the $J = 2$ peak in a level of the 2 (0^+) state in Figure 6 below.

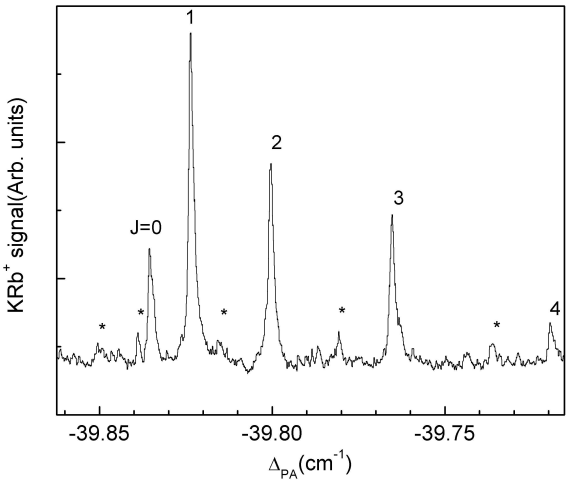

Fig. 6. High-resolution spectrum of a free-bound vibrational absorption band to the $2(0^+)$ electronic state correlating with the K($4s$) + Rb($5p_{1/2}$) limit in Figures 2 and 3. The rotational structure for $J = 0{-}4$ is clearly evident. Hyperfine "ghosts" for levels $J = 0{-}4$ are noted with an asterisk.

300 μK and 100 μK, respectively, but these have not yet been measured. The two MOTs were carefully adjusted to maximize the overlap of the two atomic clouds, which could be separately viewed by observing K($4p_{3/2} \rightarrow 4s$) and Rb($5p_{3/2} \rightarrow 5s$) trap fluorescence with narrow band filters.

Two-photon ionization at 602.5 nm is used to ionize KRb $a^3\Sigma^+$ molecules to KRb^+; we have not established whether or not KRb $X^1\Sigma^+$ molecules are ionized as well. Note that for both $X^1\Sigma^+$ and $a^3\Sigma^+$ states, most of the molecules are expected to be near the dissociation limit. The uncertainty concerning singlet detection arises because, as discussed in Section 2 (e.g. Tab. 4), all KRb electronic states formed by PA are expected to spontaneously emit to the $a^3\Sigma^+ \sim (1(0^-), 1(1))$ state, and some states ($2(0^-)$, $3(0^-)$, and $1(2)$) should do so exclusively. In the future, using the triplet trap described in Section 5 below, we hope to establish the relative efficiency for ionization of singlet and triplet molecules using the $2(0^+)$ and $2(1)$ states where the singlet/triplet branching is accurately predicted in Table 4. The fact that 0^+ states emit to both the singlet ($X^1\Sigma^+$) state and the triplet ($a^3\Sigma^+$) state, while 0^- states emit only to the triplet ($a^3\Sigma^+$) state may be useful in assigning $\pm$ symmetry.

The ionizing laser is a 10 Hz pulsed dye laser at 602.5 nm pumped by a doubled Nd:YAG laser at 532 nm. Typical ionizing laser pulses are 1.5 mJ with 10 ns duration and a typical peak intensity of 7×10^6 W/cm^2. The ions formed are accelerated in a low resolution time-of-flight mass spectrometer and detected on a channeltron. A typical mass spectrum is shown in Figure 5 and includes K^+ and Rb^+ atomic ion signals and KRb^+ and Rb_2^+ molecular ion signals, with the KRb^+ ion signal dominating and corresponding to ~60 ions/laser pulse (compared to a background of ~1.7 ions/laser pulse when our PA laser is detuned from a KRb resonance). For the spectrum in Figure 5, we used a cw tunable PA laser (Coherent 899-29, typically >400 mW, ~1 MHz jitter) detuned 39.80 cm^{-1} below the Rb ($5p_{1/2}$ $F' = 2 \rightarrow 5s$ $F'' = 2$) transition. PA spectra are obtained by varying the detuning from ~1 to 95 cm^{-1} while monitoring the KRb^+ ion signal. An example of such a PA spectrum is shown in Figure 6. KRb^+ ion signals similar to those shown in Figure 5 are also obtained with 532 nm two-photon ionization; however, 602.5 nm detection seems to be slightly more effective, and is used in all work reported below.

Our frequency measurements are all made with respect to the ^{85}Rb ($5s$, $F'' = 2$) $\rightarrow$ ($5p_{1/2}$, $F' = 2$) transition, labeled b′ in [76]. This transition is 2674.230 MHz above the accurately measured optical transition (c′) at 377106271.6 (4) MHz = 12578.91123 (1) cm^{-1}, so b′ is at 12579.00043 (1) cm^{-1}.

4 Photoassociative spectra and photoassociative molecule formation

The PA spectra for red detunings up to 95 cm^{-1} below the ^{39}K($4s$) + ^{85}Rb ($5p_{1/2}$) asymptote are shown in Figure 7. Each of the major features corresponds to a rotationally resolved free-bound vibrational band to one of the eight states correlating with the K($4s$) + Rb($5p_J$) asymptotes and is similar to the example shown in Figure 6. The three possible Ω values, 0, 1, and 2, are readily determined from the rotationally resolved spectrum, with the $\Omega = 0$ states exhibiting rotational energy proportional to $J(J+1)$ (typically from $J = 0$ to 4), the $\Omega = 1$ states proportional to $J(J+1) - 1$ (typically up to $J = 4$), and the $\Omega = 2$ states proportional to $J(J+1) - 4$ (typically up to $J = 4$). There is no evidence for significant centrifugal distortion (nonlinear behavior as a function of $J(J+1) - \Omega^2$). The distinction between 0^+ and 0^- states is not apparent from the spectra.

The observed $\Omega = 0$ levels are uniformly sharp (typical full width half maximum (FWHM) linewidths of

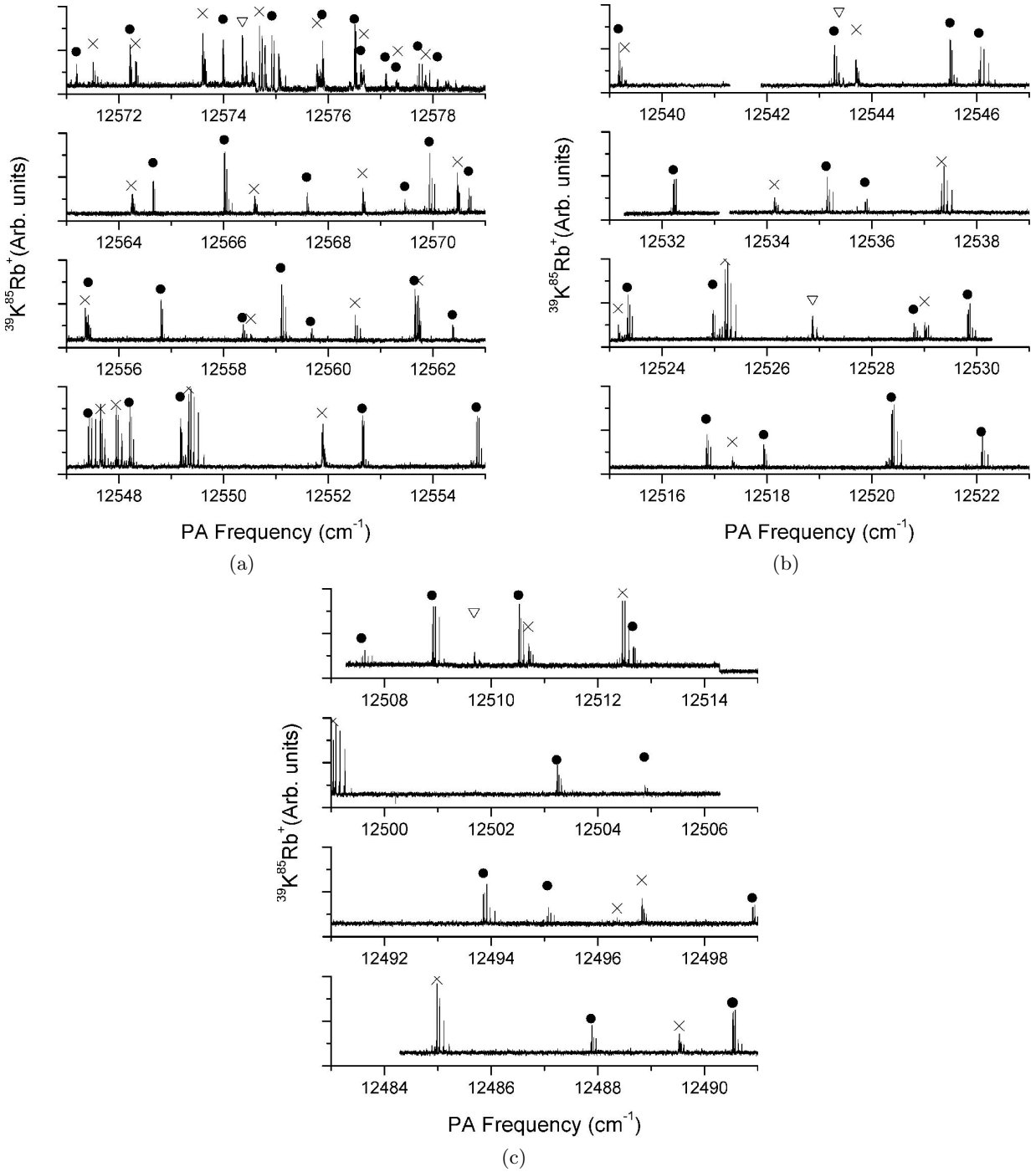

Fig. 7. Photoassociation spectra of ^{39}K^{85}Rb up to 95 cm^{-1} below the ^{39}K($4s$, $F' = 1$) + ^{85}Rb($5p_{1/2}$, $F' = 2$) asymptote detected using two-photon ionization at 602.5 nm and time-of-flight mass spectroscopy. The bands are marked: (•) $\Omega = 0$, (×) $\Omega = 1$ and (▽) $\Omega = 2$, based on their rotational structure.

0.001 cm^{-1}). $\Omega = 1$ levels are generally broader, sometimes with structure (presumably hyperfine), for which the envelope is largest for $J = 1$, decreasing for $J = 2$ and then $J = 3$ and 4. For example, Figure 8 shows a particularly broad $\Omega = 1$ band with FWHM envelope widths of ∼0.018 cm^{-1} for $J = 1$, ∼0.013 cm^{-1} for $J = 2$, and ∼0.008 cm^{-1} for $J = 3$. $\Omega = 2$ levels show significant hyperfine structure in each J level, although the width of the hyperfine envelope shrinks continuously from $J = 2$ to 3 to 4. An example of such structure is shown in Figure 9.

We expect many perturbations among these eight states for a variety of reasons, including both homogeneous ($\Delta\Omega = 0$) and heterogeneous ($\Delta\Omega = \pm 1$) perturbations. In particular, the 0^+ and 0^- states do not directly

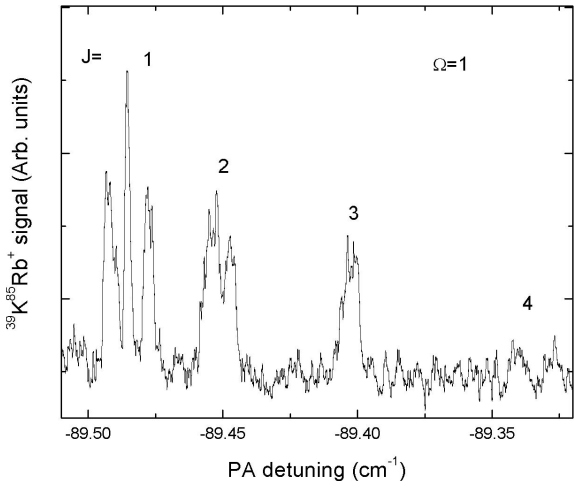

Fig. 8. PA spectrum of an $\Omega = 1$ band at $\Delta_{PA} = -89.48$ cm^{-1} showing significant structure (presumably hyperfine).

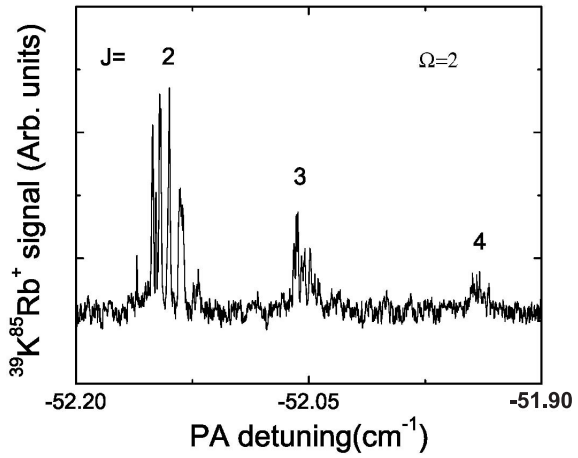

Fig. 9. PA spectrum of an $\Omega = 2$ band at $\Delta_{PA} = -52.14$ cm^{-1} showing significant structure (presumably hyperfine).

perturb each other or the 1(2) state; however, the 1 states perturb (and are perturbed by) all other states. Asymptotically (Fig. 2), the $2(0^+)$, 2(1), and $2(0^-)$ states converging to the same asymptote (the lower triad) most strongly perturb each other; for the upper K($4s$) + Rb($5p_{3/2}$) asymptote, two groups of states are formed, the dyad (1(2), 4(1)) and the upper triad ($3(0^+)$, $3(0^-)$, 3(1)), where the perturbations among states in a group will be stronger than those between states in different groups. At intermediate distances (Fig. 3), however, there are strong perturbations among the 1(2), 3(1), $3(0^+)$, $3(0^-)$, 2(1), and $2(0^-)$ states, which become the $1^3\Pi$ and $2^3\Sigma^+$ states at short distance. At small distance (Fig. 1), the $A^1\Sigma^+$ ($\sim 2(0^+)$) and $1^3\Pi_{0^+}$ ($\sim 3(0^+)$) states cross, giving an additional perturbation. The $1^1\Pi \sim 4(1)$ and $2^1\Pi \sim 5(1)$ states perturb each other at short distance and are predissociated at and above the K($4s$) + Rb($5p_{1/2}$) asymptote by the $2^3\Sigma^+ \sim 2(0^-)$, 2(1) state [48]. Thus the final resolution and assignment of the many levels of the eight states we have observed will ultimately involve a detailed calculation including all of these perturbations. Many levels will have significant

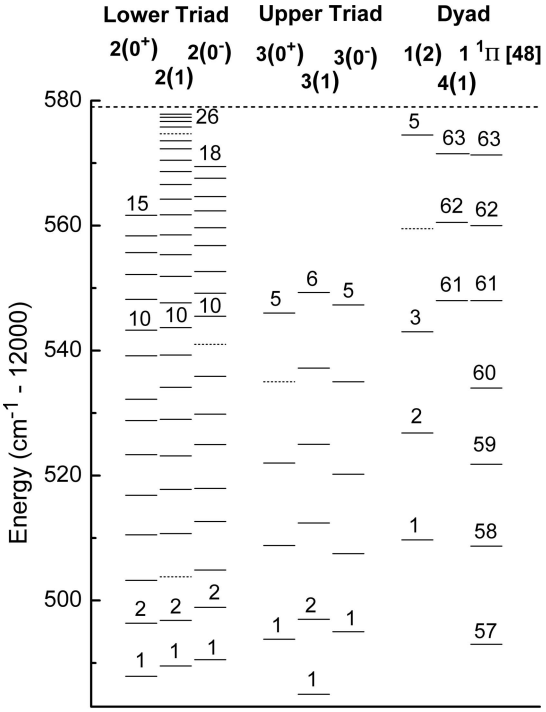

Fig. 10. Energy level diagrams for the levels of the $2(0^+)$, 2(1), and $2(0^-)$ states of $^{39}K^{85}Rb$ converging toward the K($4s$) + Rb($5p_{1/2}$) asymptote (indicated by the horizontal dashed line at 12579.00 cm^{-1}), of the $3(0^+)$, 3(1), and $3(0^-)$ states and of the 4(1) and 1(2) states, correlating to the K($4s$) + Rb($5p_{3/2}$) asymptote. For the $4(1) \sim 1^1\Pi$ state, the results from conventional short-range spectroscopy [48] are also given in the right most column.

character from more than one electronic state. Nevertheless, we feel it is useful to make preliminary assignments of these many levels, as shown in Figure 10.

One key to making the assignments shown in Figure 10 is the spectral region (12545.4−12549.8 cm^{-1}) shown in Figure 11. The two features labeled $2(0^-)$ correspond to strong vibrational bands (in Fig. 7) and are part of a long vibrational series with binding energies characteristic of R^{-6} long range behavior (Fig. 12). They have some of the smallest rotational constants (proportional to expectation values of R^{-2}) of any vibronic levels in Figure 11, as expected (from Fig. 3) for the longest range levels, and as observed in other members of the long vibrational series (see Fig. 10). The other two small rotational constants correspond to the $2(0^+)$ and 2(1) levels, respectively. The $2(0^+)$ and 2(1) levels are also members of long vibrational series showing R^{-6} long-range behavior (Fig. 12), and other members of these long series also show small rotational constants. From Figure 3, we expect that the other two $\Omega = 0$ levels ($3(0^+)$ and $3(0^-)$) and other $\Omega = 1$ levels (3(1) and 4(1)) will have much larger rotational constants. We also note that the states with the highest density of levels (i.e. smallest vibrational spacings) in Figure 10 are the $2(0^+)$, $2(0^-)$ and 2(1) states, and that therefore, for any of the $\Omega = 0$ or 1 states other than $2(0^-)$, no second vibrational band in Figure 11 will

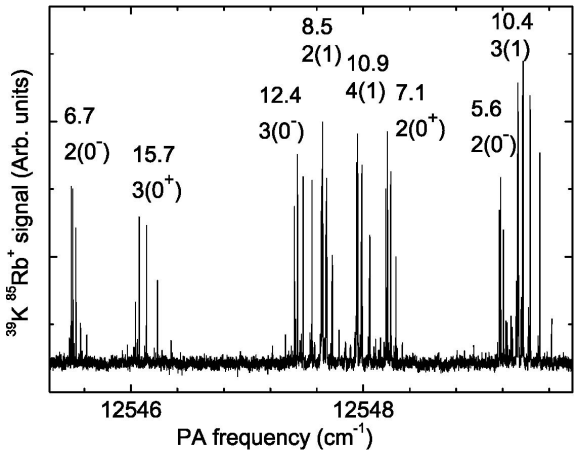

Fig. 11. PA spectrum for $^{39}K^{85}Rb$ showing eight vibrational bands (from seven electronic states) in the region 12545.3−12549.8 cm^{-1}. The preliminary state number and $\Omega^{(\pm)}$ symmetry is given for each band. It should however be noted that many of the observed levels are strongly perturbed and thus not well represented by a single vibronic state. Also given above the symmetry is $10^3 B_v$ in cm^{-1}, with smaller B_v corresponding to a more long-range level, i.e. a level with a larger outer turning point. All eight state symmetries (including $\Omega = 2$, not occurring in this region) can be reached by dipole-allowed transitions from colliding ground state atoms ($\Omega = 0^{\pm}$, 1).

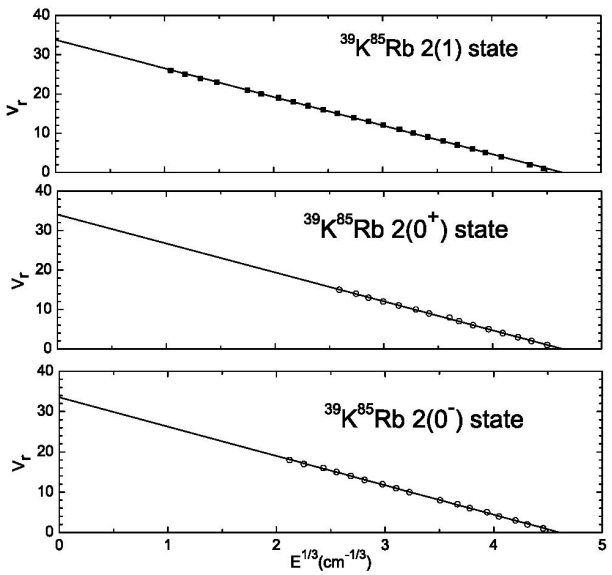

Fig. 12. Plot of the relative vibrational quantum number v_R versus the cube root of the binding energy in cm^{-1} (magnitude of the detuning) for the $2(0^+)$, 2(1), and $2(0^-)$ vibrational series ($J = \Omega$ levels) shown in Figures 7 and 10. The levels are numbered up from the lowest observed level (1). The lines correspond to best fits with parameters given in Table 5.

Table 5. Effective C_6 and v_D values for the $2(0^+)$, $2(0^-)$, and 2(1) states of $^{39}K^{85}Rb$.

state	C_6 (a.u.)	v_D
$2(0^+)$	$(1.06 \pm 0.06) \times 10^5$	$v_R^{0^+} + 34.1 \pm 0.1$
$2(0^-)$	$(1.01 \pm 0.04) \times 10^5$	$v_R^{0^-} + 33.6 \pm 0.2$
2(1)	$(1.01 \pm 0.05) \times 10^5$	$v_R^1 + 33.8 \pm 0.1$

correspond to the same electronic state, i.e. $2(0^+)$, $3(0^+)$, $3(0^-)$, 3(1), and 4(1) bands occur once and only once in this spectral region.

A second key to the assignments shown in Figure 10 is the lower triad ($2(0^+)$, $2(0^-)$, 2(1)) — upper triad ($3(0^+)$, $3(0^-)$, 3(1)) — dyad (4(1), 1(2)) concept discussed above. Within each group, the levels have nearly the same C_6 values and thus have similar vibrational spacings and similar rotational constants. Note how in the lower triad, the groups of three lower triad levels within a few cm^{-1} tend to follow the order of binding energies $E_{v_R}(2(0^+)) > E_{v_R}(2(1)) > E_{v_R}(2(0^-))$, where v_R is the relative vibrational quantum number, starting with $v_R = 1$ for the $2(0^+)$ level at 12487.9 cm^{-1}, the 2(1) level at 12489.5 cm^{-1} and the $2(0^-)$ level at 12490.5 cm^{-1}, and continuing up to $v_R = 15$ with only a few missing levels. Note also that for $v_R \geq 13$, the $2(0^+)$ and 2(1) bands are close or overlapping. We assign one $\Omega = 0$ series as $2(0^+)$ and one as $2(0^-)$ based on the relative C_6 values predicted (Tab. 3) and observed (Tab. 5).

The dyad (4(1), 1(2)) is next easiest to assign. Long-range theory is breaking down at the shorter distances involved (outer turning points of $\sim 17a_0$). However, the $\Omega = 2$ levels have unique structure (Fig. 9) and we have readily identified four levels. For the 4(1) state, we can take advantage of the previous "short-range" observations of [48], shown in Table 1. We observe 4(1) levels (v = 63, 62, 61) with binding energies of 7.6, 18.5 and 31.1 cm^{-1}, in good agreement with 7.88, 19.23, and 31.48 (each ± 0.42 cm^{-1}) in Table 1. We note that in all levels seen in [48], high J data ($J \geq 20$) is extrapolated to $J = 1$ to obtain T_v and B_v, with significant uncertainty. The B_v values we observe do tend to be significantly smaller than those obtained in [48]; for v = 61−63, we observe $10^3 B_v$ (cm^{-1}) of 11.3, 9.9 and 8.5, respectively, compared to 13.9, 13.3 and 13.6 in [48]. We hope to directly compare and combine our data with those of [48] in a future analysis, which directly ties together long-range and short-range data (as in [77] for the $1^1\Pi_g$ state of $^{39}K_2$).

Finally, we turn to the upper triad ($3(0^+)$, $3(0^-)$, 3(1)). The $\Omega = 1$ assignments are straightforward, given the analyses of the 2(1) and 4(1) states above. There are six regularly spaced, large rotational constant vibrational levels we assign to the 3(1) state. We then group with these the remaining $\Omega = 0$ vibrational levels, as shown in Figure 10. The $3(0^-)$ state is predicted to have the largest of the similar C_6 values, then 3(1) and then $3(0^+)$. We would expect $3(0^-)$ to have the largest outer turning point and thus the smallest rotational constant, with 3(1) next and $3(0^+)$ last. We assign the 0^+ and 0^- states on this basis in Figure 10. There are many additional levels of the $\Omega = 0$ states ($3(0^+)$ or $3(0^-)$) but few levels of the 3(1) state above 12550 cm^{-1} and we have not yet fully assigned them.

It is also worthwhile to briefly consider the question of predissociation of the five upper states (correlating to K($4s$) + Rb($5p_{3/2}$)) to the K($4s$) + Rb($5p_{1/2}$) asymptote. It would appear that there are many predissociation opportunities for four of the five higher asymptote states: the $3(0^+)$ state by mixing with the $2(0^+)$ state at short range, or by mixing with the 2(1) state near $12a_0$; the $3(0^-)$ state by mixing with the $2(0^-)$ and 2(1) states near $12a_0$; the 3(1) state by mixing with the 2(1) and $2(0^-)$ states near $12a_0$; and the 1(2) state by mixing with the 2(1) state near $12a_0$. Even the 4(1) state, which should be the most immune to predissociation, is slightly mixed with the 1(2) state asymptotically, so a weak predissociation is possible. Indeed such a weak predissociation of the $1^1\Pi \sim 4(1)$ state (and the $2^1\Pi \sim 5(1)$ state to which it is coupled) has been observed as line broadening [48]. No heteronuclear spectra involving the upper asymptote have been observed either in our work on KRb or in the prior work on RbCs [29,30]. However, the "background" molecules formed in our work and in that of Mancini et al. [34] presumably originate from very long-range PA due to the MOT lasers with transition frequencies near the Rb($5s \rightarrow 5p_{3/2}$) transition.

The long vibrational series plotted in Figure 12 were fit to the semiclassical equation [78,79]:

$$v_D - v = \frac{4a_n}{h(n-2)}\sqrt{2\mu}C_n^{1/n}E_v^{(n-2)/2n} \quad (1)$$

with

$$a_n = \frac{\sqrt{\pi}}{2}\frac{\Gamma(1/2+1/n)}{\Gamma(1+1/n)} \quad (2)$$

where here $n = 6$, corresponding to a long-range $-C_6R^{-6}$ attractive potential, v_D is the vibrational quantum number at dissociation (typically noninteger), v is the vibrational quantum number, h is Planck's constant, μ is the reduced mass (here of $^{39}K^{85}Rb$), and E_v is the binding energy of the level v (equal to the magnitude of the detuning $|\Delta_v|$). From our linear fits of $v_D - v$ versus $(E_v)^{1/3}$ in Figure 12, we obtain C_6 and v_D, as listed in Table 5.

We note that these fits are approximate. In addition to statistical uncertainties and neglect of $-C_8R^{-8}$ and higher dispersion terms, it should be noted that these C_6 values are effective C_6 values, since C_6 in fact is expected to vary slowly with R. For example, in the calculations of Bussery et al. [65] (Tab. 3), $C_6(2(0^+))$ varies from 1.03×10^5 a.u. at very long range (spin-orbit splitting $\gg$ dispersion) to 3.06×10^5 a.u. at intermediate range (spin-orbit $\ll$ dispersion). The values we report are moderately long-range ones close to the very long range limit; they are most appropriate for our range of detunings, and will fairly well reproduce the energy levels used in our fits and predict the energies of the many unobserved levels above those we have observed.

5 Magnetic trapping of KRb a $^3\Sigma^+$ molecules

We have observed trapping of metastable KRb molecules in the magnetic field gradient of the MOT coils, which has a typical value of 28 Gauss/cm. Analogous magnetic trapping has previously been reported for Cs_2 [13] and for Rb_2 [80], although not for heteronuclear molecules. Only molecules in the metastable $a^3\Sigma^+$ state can be magnetically trapped, since molecules in the $X^1\Sigma^+$ ground state have negligible magnetic moments. We investigated the trapping by turning off the PA laser while leaving the MOT lasers and magnetic field on, then firing a detection laser pulse after a variable delay. Figure 13 shows the decay of the KRb^+ ion signal as a function of this delay, with the laser tuned to a strong KRb resonance to the $3(0^-)$ state. We have subtracted a constant background of 1.7 ions/shot due to "spontaneous" formation of KRb by the trap laser alone. It is evident that the decay is non-exponential, with a significant fraction of the KRb molecules remaining long after the ballistic decay time. To model the ballistic decay quantitatively we have used Monte Carlo simulations, which show an initial decay time constant of about 3.2 ms for our 1 mm diameter detection beam, assuming a temperature of $\sim$300 μK. These simulations also predict a small longer-lived tail attributable to molecules that form a "molecular fountain" by initially moving upwards and later re-entering the detection region. However, the size of this tail is much smaller than the observed signals past 10 ms, and it vanishes almost entirely within 30 ms. By contrast, the longest-lived component of the ion signal survives for hundreds of milliseconds.

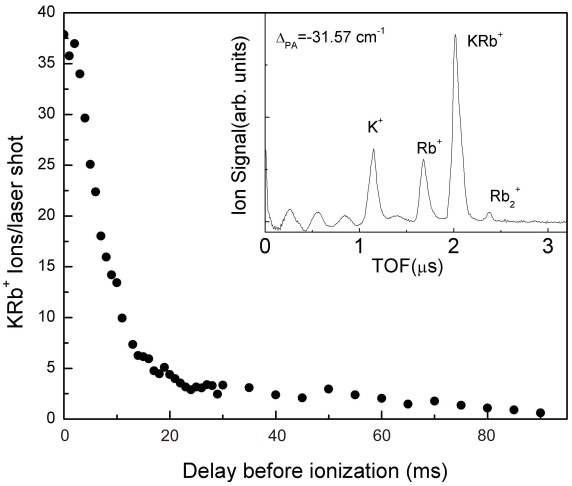

Fig. 13. KRb^+ ion signal (arbitrary units) as a function of the delay (in ms) between turning off the PA laser (while leaving the MOT lasers and the magnetic field on) and firing a detection laser pulse [40].

The dynamics of this trap are somewhat complex because the atoms in the MOT are unpolarized. The triplet molecules formed have a wide distribution of magnetic moments ranging from -2 Bohr magnetons (μ_0) to $+2\mu_0$, because of the statistical distribution of projection quantum numbers, either m_J or m_F depending on the applicable angular momentum coupling scheme. About 1/3 of the molecules should be in low-field seeking states that can in principle be trapped, but these molecules have a wide distribution in effective trapping potentials, resulting in

an inhomogeneous distribution of trap sizes and escape rates for different molecules. In Figure 13, about 10% of the initial molecular signal survives past 30 ms. This indicates a rather low trapping efficiency compared to the upper bound of 33%, because the long holding time of the trap should enhance the trapped molecule signal by more than an order of magnitude relative to the short-lived component that dominates the decay curve at short detection delay times. For a molecule with the largest possible dipole moment projection of $2\mu_0$, the trapping potential in the horizontal plane reaches a depth of $\sim$500 μK at a radius of 2.5 mm. As we expect the temperature of the initial molecular distribution to be somewhere in the range 150−400 μK, most of the successfully trapped molecules should be confined within this radius. In the vertical direction gravity causes some distortion, as the maximum magnetic force is only 2.5 times larger than the gravitational force. Additional experimental work is presently underway to investigate the details of the trapping dynamics.

6 Future prospects

In the future, we hope to complete our study of KRb photoassociation near the K($4s$) + Rb ($5p_J$) asymptotes in several ways. One way is to fill gaps in our K($4s$) + Rb ($5p_{1/2}$) observations, e.g. the missing levels in Figure 10. More importantly, we hope to carry out model calculations of the levels (including the many perturbations), similar, for example, to those discussed in K_2 [77] and RbCs [29]. In this way we can confirm the preliminary assignments of Section 4. Some isotopic experiments (e.g. ^{39}K^{87}Rb) might be required.

We also plan to examine the levels between the two asymptotes, where predissociation to form Rb($5p_{1/2}$) atoms is possible. We will use molecular ionization detection (as here), trap loss, and resonance-enhanced multiphoton ionization (REMPI) of the Rb($5p_{1/2}$) atoms. We have previously examined similar predissociations with REMPI in $^{39}K_2$ [81].

We will use our trap to attempt to determine the relative sensitivity for detection of singlet molecules and triplet molecules by PA to 1 (or 0^+) levels. If detection of singlet molecules is not adequately sensitive at 602.5 nm, we will try other nearby wavelengths. We will also attempt to confirm that specific levels are 0^+ or 0^- by detecting the occurrence or nonoccurrence of emission to the singlet $X^1\Sigma^+$ state.

Finally we will use our existing CO_2 laser system to produce a tighter trap for KRb molecules in order to carry out collisional experiments.

It is interesting to examine the prospects for study of ultracold collisions and chemical reactions of $X^1\Sigma^+$ ^{39}K^{85}Rb ($v = 0$, $J = 0$). We assume that, as is commonly believed for alkali atom and alkali dimer reactions, there is no barrier to reaction on the ground doublet potential energy surface. For example, the reaction

$$^{39}\mathrm{K}^{85}\mathrm{Rb}(v=0,J=0)+{}^{39}\mathrm{K}\rightarrow{}^{39}\mathrm{K}_2(v',J')+{}^{85}\mathrm{Rb} \quad (3)$$

is exoergic by 224.80 ± 0.52 cm^{-1} (based on $D_0 = 4180.06 \pm 0.42$ cm^{-1} for ^{39}K^{85}Rb [54] and $D_0 = 4404.86 \pm 0.30$ cm^{-1} for $^{39}K_2$ [77]). Energetically, this means that $v' \leq 2$ and $J' \leq 63$ could be produced. However, with the reaction occurring on a doublet surface with $S = 1/2$ conserved, we expect

$$\vec{J}+\vec{\ell}\cong 0\cong\vec{J}'+\vec{\ell}' \quad (4)$$

where $\vec{\ell}$ is the entrance channel angular momentum of collision ($\ell \leq 3$ at 300 μK) and $\vec{\ell}'$ is the exit channel angular momentum of collision. Thus highest J' levels (such as $J' = 63$) cannot be formed since they cannot pass over the ℓ' exit channel angular momentum barrier, i.e. because of angular momentum rather than energetic constraints.

On the other hand, the reaction

$$^{39}\mathrm{K}^{85}\mathrm{Rb}\,(v=0,J=0)+{}^{85}\mathrm{Rb}\rightarrow{}^{85}\mathrm{Rb}_2(v'=0,J'=0)+{}^{39}\mathrm{K} \quad (5)$$

is endoergic by 214.60 ± 0.50 cm^{-1} and will not occur at ultracold temperatures. If higher vibrational levels v are excited, e.g. $v = 3$, $J = 0$, the corresponding reaction

$$^{39}\mathrm{K}^{85}\mathrm{Rb}(v=3,J=0)+{}^{85}\mathrm{Rb}\rightarrow{}^{85}\mathrm{Rb}_2(v'=0,J'=0)+{}^{39}\mathrm{K} \quad (6)$$

is now exoergic by 48.01 ± 0.50 cm^{-1} and J' levels up to 49 can be produced in place of $J' = 0$ energetically; however, the exit kinetic energy for $X^1\Sigma_g^+$ $^{85}Rb_2$, $v' = 0$, $J' = 49$ is only 1.25 cm^{-1} (<2 K) which certainly could not overcome a centrifugal barrier corresponding to $\ell' > 40$.

Finally, inelastic collisions could be readily studied, particularly with ^{85}Rb where reaction is energetically forbidden; for example, rotational relaxation

$$^{39}\mathrm{K}^{85}\mathrm{Rb}(v=0,J=1)+{}^{85}\mathrm{Rb}\rightarrow{}^{39}\mathrm{K}^{85}\mathrm{Rb}(v'=0,J'=0)+{}^{85}\mathrm{Rb} \quad (7)$$

or vibrational relaxation

$$^{39}\mathrm{K}^{85}\mathrm{Rb}(v=1,J=0)+{}^{85}\mathrm{Rb}\rightarrow{}^{39}\mathrm{K}^{85}\mathrm{Rb}(v'=0,J')+{}^{85}\mathrm{Rb} \quad (8)$$

where J' levels up to 44 can be produced energetically, but where the small exit kinetic energy for $J' = 44$ is 0.15 cm^{-1} ($\sim$0.2 K), so again the exit channel centrifugal barrier will prevent completion of the inelastic collision forming $J' = 44$.

Studies such as those mentioned above could be readily carried out using a state-selected sample of ^{39}K^{85}Rb. The use of a Feshbach resonance to produce a very weakly bound (predominantly) triplet $a^3\Sigma^+$ level, followed by stimulated Raman scattering via the intermediate $A^1\Sigma^+ \sim b^3\Pi$ mixed singlet-triplet levels to the $X^1\Sigma^+$ ^{39}K^{85}Rb $v = 0$, $J = 0$ level (or 3, 0; 0, 1; or 1, 0) is a very promising approach for preparing such a state-selected sample [27].

We gratefully acknowledge support from the National Science Foundation (PHY-9987762 and PHY-0354869), the North Atlantic Treaty Organization Science for Peace Program and the University of Connecticut Foundation and participation in the European Community Research Training Network on Cold Molecules (with NSF support). We also gratefully acknowledge helpful discussions with Jamie Kerman, David DeMille, Tom Bergeman, Olivier Dulieu, Marjatta Lyyra and Svetlana Kotochigova, and laboratory assistance from Andrew Scott and Ye Huang.

References

1. J. Weiner, V.S. Bagnato, S.C. Zilio, P.S. Julienne, Rev. Mod. Phys. **71**, 1 (1999)
2. W.D. Phillips, Rev. Mod. Phys. **70**, 721 (1998)
3. S. Chu, Rev. Mod. Phys. **70**, 685 (1998)
4. C.N. Cohen-Tannoudji, Rev. Mod. Phys. **70**, 707 (1998)
5. W. Ketterle, Rev. Mod. Phys. **74**, 1131 (2002)
6. E.A. Cornell, C.E. Wieman, Rev. Mod. Phys. **74**, 875 (2002)
7. A. Fioretti, D. Comparat, A. Crubellier, O. Dulieu, F. Masnou-Seeuws, P. Pillet, Phys. Rev. Lett. **80**, 4402 (1998)
8. J.T. Bahns, P.L. Gould, W.C. Stwalley, Adv. At. Mol. Opt. Phys. **42**, 171 (2000)
9. W.C. Stwalley, H. Wang, J. Mol. Spectrosc. **195**, 194 (1999)
10. F. Masnou-Seeuws, P. Pillet, Adv. At. Mol. Opt. Phys. **47**, 53 (2001)
11. U. Schlöder, C. Silber, C. Zimmermann, Appl. Phys. B. **73**, 801 (2001)
12. T. Takekoshi, B.M. Patterson, R.J. Knize, Phys. Rev. Lett. **81**, 5105 (1998)
13. N. Vanhaecke, W. de Souza Melo, B.L. Tolra, D. Comparat, P. Pillet, Phys. Rev. Lett. **89**, 063001 (2002)
14. J. Herbig, T. Kramer, M. Mark, T. Weber, C. Chin, H.-C. Nägerl, R. Grimm, Science **301**, 1510 (2003)
15. C.C. Chin, A.J. Kerman, V. Vuletic, S. Chu, Phys. Rev. Lett. **90**, 033201 (2003)
16. S. Dürr, T. Volz, A. Marie, G. Rempe, Phys. Rev. Lett. **92**, 020406 (2004)
17. K. Xu, T. Mukaiyama, J.R. Abo-Shaeer, J.K. Chin, D.E. Miller, W. Ketterle, Phys. Rev. Lett. **91**, 210402 (2003)
18. S. Jochim, M. Bartenstein, A. Altmeyer, G. Hendl, S. Riedl, C. Chin, J. Hecker Denschlag, R. Grimm, Science **302**, 2101 (2003)
19. J. Cubizolles, J. Bourdel, S.J.J.M.F. Kokkelmans, G.V. Shlyapnikov, C. Salomon, Phys. Rev. Lett. **91**, 240401 (2003)
20. K.E. Strecker, G.B. Partridge, R.G. Hulet, Phys. Rev. Lett. **91**, 080406 (2003)
21. M.W. Zwierlein, C.A. Stan, C.H. Schunk, S.M.F. Raupach, S. Gupta, Z. Hadzibabic, W. Ketterle, Phys. Rev. Lett. **91**, 250401 (2003)
22. C.A. Regal, C. Ticknor, J.L. Bohn, D.S. Jin, Nature **424**, 47 (2003)
23. M. Greiner, C.A. Regal, D.S. Jin, Nature **426**, 537 (2003)
24. D.S. Petrov, C. Salomon, G.V. Shlyapnikov, Phys. Rev. Lett. **93**, 090404 (2004)
25. W.C. Stwalley, in *State-to-State Chemistry*, edited by P.R. Brooks, E.F. Hayes, Am. Chem. Soc. Symp. Ser. **56**, 247 (1977)
26. W.C. Stwalley, Can. J. Chem. **82**, 1 (2004)
27. W.C. Stwalley, Eur. J. Phys. D **31**, 221 (2004)
28. H. Wang, W.C. Stwalley, J. Chem. Phys. **108**, 5767 (1998)
29. A.J. Kerman, J.M. Sage, S. Sainis, T. Bergeman, D. DeMille, Phys. Rev. Lett. **92**, 033004 (2004)
30. A.J. Kerman, J.M. Sage, S. Sainis, T. Bergeman, D. DeMille, Phys. Rev. Lett. **92**, 153001 (2004)
31. T. Bergeman, A.J. Kerman, J. Sage, S. Sainis, D. DeMille, Eur. J. Phys. D **31**, 179 (2004)
32. J.P. Shaffer, W. Chalupczak, N.P. Bigelow, Phys. Rev. Lett. **82**, 1224 (1999)
33. H. Wang, Bull. Am. Phys. Soc. **48**, J1.025 (2003)
34. M.W. Mancini, G.D. Telles, A.R.L. Caires, V.S. Bagnato, L.G. Marcassa, Phys. Rev. Lett. **92**, 133203 (2004)
35. S. Inouye, J. Goldwin, M.L. Olsen, C. Ticknor, J.L. Bohn, D.S. Jin, Phys. Rev. Lett. **93**, 183201 (2004)
36. C.A. Stan, M.W. Zwierlein, C.H. Schunck, S.M.F. Raupach, W. Ketterle, Phys. Rev. Lett. **93**, 143001 (2004)
37. J.D. Weinstein, R. DeCarvalho, T. Guillet, B. Friedrich, J.M. Doyle, Nature **395**, 148 (1998)
38. H.L. Bethlem, G. Berden, F.M.H. Crompvoets, R.T. Jongma, A.J.A. Van Roij, G. Meijer, Nature **406**, 491 (2000)
39. F.M.H. Crompvoets, H.L. Bethlem, R.T. Jongma, G. Meijer, Nature **411**, 174 (2001)
40. D. Wang, J. Qi, M.F. Stone, O. Nikolayeva, H. Wang, B. Hattaway, S.D. Gensemer, P.L. Gould, E.E. Eyler, W.C. Stwalley, preprint `arXiv:physics/0410220`
41. J.M. Walter, S. Barratt, Proc. Roy. Soc. Lond. **119**, 257 (1928)
42. K.P. Huber, G. Herzberg, *Molecular Spectra and Molecular Structure IV. Constants of Diatomic Molecules* (Van Nostrand, NY, 1979)
43. J.C. Whitehead, R. Grice, Faraday Discuss. Chem. Soc. **55**, 320 (1973)
44. R. Beuc, S. Milosevic, G. Pichler, J. Phys. B **17**, 739 (1984)
45. H. Skenderović, R. Beuc, T. Ban, G. Pichler, Eur. Phys. J. D **19**, 49 (2002)
46. A.J. Ross, C. Effantin, P. Crozet, E. Boursey, J. Phys. B **23**, L247 (1990)
47. N. Okada, S. Kasahara, T. Ebi, M. Baba, H. Katô, J. Chem. Phys. **105**, 3458 (1996)
48. S. Kasahara, C. Fujiwara, N. Okada, H. Katô, J. Chem. Phys. **111**, 8857 (1999)
49. C. Amiot, J. Verges, C. Effantin, J. d'Incan, Chem. Phys. Lett. **321**, 21 (2000)
50. C. Amiot, J. Verges, J. Chem. Phys. **112**, 7068 (2000)
51. C. Amiot, J. Verges, J. d'Incan, C. Effantin, Chem. Phys. Lett. **315**, 55 (1999)
52. C. Amiot, J. Mol. Spectrosc. **203**, 126 (2000)
53. Y. Lee, C. Yun, Y. Yoon, T. Kim, B. Kim, J. Chem. Phys. **115**, 7413 (2001)
54. W.C. Stwalley, J. Chem. Phys. (2004, submitted)
55. S. Rousseau, A.R. Allouche, M. Aubert-Frécon, J. Mol. Spectrosc. **203**, 235 (2000)
56. S.J. Park, Y.J. Choi, Y.S. Lee, G.-H. Jeung, Chem. Phys. **257**, 135 (2000)
57. S. Kotochigova, P.S. Julienne, E. Tiesinga, Phys. Rev. A **68**, 022501 (2003)
58. A. Derevianko, J.F. Babb, A. Dalgarno, Phys. Rev. A **63**, 052704 (2001)
59. S.G. Porsev, A. Derevianko, J. Chem. Phys. **119**, 844 (2003)

60. W.T. Zemke, W.C. Stwalley, J. Chem. Phys. **120**, 88 (2004)
61. W.T. Zemke, R. Côté, W.C. Stwalley, Phys. Rev. A (2004, to be submitted)
62. M. Marinescu, H.R. Sadeghpour, Phys. Rev. A **59**, 390 (1999)
63. W.T. Zemke, W.C. Stwalley, Phys. Rev. A (2004, to be submitted)
64. M. Movre, R. Beuc, Phys. Rev. A **31**, 2957 (1984)
65. B. Bussery, Y. Achkar, M. Aubert-Frécon, Chem. Phys. **116**, 319 (1987)
66. M.T. Djerad, F. Gounand, A. Kumar, M. Cheret, J. Chem. Phys. **97**, 8334 (1992)
67. C. Gabbanini, M. Biagini, S. Gozzini, A. Lucchesini, A. Kopystynska, J. Quant. Spectrosc. Radiat. Transfer **47**, 103 (1992)
68. C. Vadla, S. Knezovic, M. Movre, J. Phys. B **25**, 1337 (1992)
69. L.G. Marcassa, G.D. Telles, S.R. Muniz, V.S. Bagnato, Phys. Rev. A **63**, 013413 (2001)
70. G. Ferrari, M. Inguscio, W. Jastrzebski, G. Modugno, G. Roati, A. Simoni, Phys. Rev. Lett. **89**, 053202 (2002)
71. J. Goldwin, S.B. Papp, B. DeMarco, D.S. Jin, Phys. Rev. A **65**, 021402 (2002)
72. G. Modugno, G. Roati, F. Riboli, F. Ferlaino, R.J. Brecha, M. Inguscio, Science **297**, 2240 (2002)
73. M.S. Stone, M.S. thesis, SUNY Stony Brook 2001
74. H. Wang, P.L. Gould, W.C. Stwalley, Phys. Rev. A **53**, R1216 (1996)
75. W. Ketterle, K. Davis, M. Joffe, A. Martin, D.E. Pritchard, Phys. Rev. Lett. **70**, 2253 (1993)
76. G. Barwood, P. Gill, W.R.C. Rowley, Appl. Phys. B **53**, 142 (1991)
77. M. Pichler, H.M. Chen, H. Wang, W.C. Stwalley, A.J. Ross, F. Martin, M. Aubert-Frécon, I. Russier-Antoine, J. Chem. Phys. **118**, 7837 (2003)
78. R.J. Le Roy, R.B. Bernstein, J. Chem. Phys. **52**, 3869 (1970)
79. W.C. Stwalley, Chem. Phys. Lett. **6**, 241 (1970)
80. C. Ryu, R.S. Freeland, R. Wynar, D. Comparat, D.J. Heinzen, abstract for Cold Molecules 2002, Les Houches, France (unpublished); also R.S. Freeland, Ph.D. thesis, University of Texas, pp. 112-122 (2001)
81. H. Wang, P.L. Gould, W.C. Stwalley, Phys. Rev. Lett. **80**, 476 (1998)